

## Impact of impurities in shielding material on simulations of instrument background in space

Michael W. J. Hubbard<sup>✉</sup>,\* David Hall, Oliver Hetherington, Timothy Arnold, and Andrew Holland

The Open University, School of Physical Sciences, Centre for Electronic Imaging, Milton Keynes, United Kingdom

---

**ABSTRACT.** A major source of background for x-ray focal plane detectors in space instrumentation aboard missions, such as Extended Roentgen Survey with an Imaging Telescope Array and Athena Wide Field Imager, is the space radiation environment. High-energy radiations from the environment interact with the spacecraft structure leading to large productions of secondary particles with energies that are detectable in the science region of interest for instrumentation. Reducing the background from these events is vital for the success of many missions. Graded-Z shielding is a common solution to help reduce the instrument background. Layers of materials with decreasing atomic numbers near detectors help reduce the background. Much of the design is determined through iterative simulations to find an optimal solution that meets the requirements for the scientific operation of the instrument. Recent results have indicated an underestimate in the instrument background from the simulations. One hypothesis has been that the simulations do not typically include the impurities in the shielding materials. The work presented investigates the association of impurities in the graded-Z materials and the instrument background spectra. Typically, impurities are not included in material definitions as they can significantly increase computational time. The impurities, percentage loading, and distribution have all been explored and evaluated for an Al-Mo-Be graded-Z shield.

© The Authors. Published by SPIE under a Creative Commons Attribution 4.0 International License. Distribution or reproduction of this work in whole or in part requires full attribution of the original publication, including its DOI. [DOI: [10.1117/1.JATIS.9.3.034004](https://doi.org/10.1117/1.JATIS.9.3.034004)]

**Keywords:** instrument background; fluorescence; impurities; device simulation; x-ray imaging; x-ray astronomy

Paper 23006G received Jan. 12, 2023; revised Jun. 8, 2023; accepted Jul. 8, 2023; published Jul. 26, 2023.

---

### 1 Introduction

Placing astronomical observatories outside the Earth's atmosphere reduces downtime due to meteorological and atmospheric conditions and enables a wider range of the electromagnetic (EM) spectrum to be explored. This includes the ability to create observatory systems that perform x-ray imaging. However, moving outside of the Earth's atmosphere presents its own set of risks and challenges. The silicon-based detectors used for x-ray imaging on Earth predominantly do not have to contend with a high natural radiation background in the science region of interest (ROI). The radiation environment in space varies based on the spacecraft's orbit and solar cycle. The impact of the environment is dependent on the spacecraft design and detector type. One of the measurable effects of these space-based radiation sources is known as instrument background radiation. The background can either be a result of direct interaction with the radiation source or

---

\*Address all correspondence to Michael W. J. Hubbard, [michael.hubbard@open.ac.uk](mailto:michael.hubbard@open.ac.uk)

from the interaction with the secondaries produced from primary radiation interaction with mass objects surrounding the detector.

Mitigating and minimizing the instrument background in the science ROI for the mission is a vital part of the spacecraft and instrumentation design. Strategies to reduce the background are centered around shielding techniques. These techniques can be split into active solutions, such as magnetic diverters and plasma shields or passive solutions utilizing bulk shielding.<sup>1–3</sup> For these strategies, solutions are carefully chosen to reduce weight and minimize other issues, such as material outgassing. A common shielding method for x-ray devices is to use multiple layers of materials with different atomic numbers laminated together. A usual configuration is to have a material gradient with the atomic number  $Z$  decreasing the closer the material is to the detector.<sup>4,5</sup> This is known as graded- $Z$  shielding and has been used on many missions and instruments including Extended Roentgen Survey with an Imaging Telescope Array (eROSITA) and Swift.<sup>6,7</sup>

The shielding solutions are tailored for each mission to allow the detectors to achieve their science goals.<sup>8</sup> These solutions are usually designed and evaluated in Monte-Carlo simulation environments, such as Geant4 and FLUKA.<sup>9,10</sup> Validations of the simulations are performed in laboratory experiments, often at mono-energetic beam lines, to achieve the high energies associated with space radiation.

The primary instrument onboard the Spectrum-Roentgen-Gamma Space Observatory is eROSITA. The instrument included graded- $Z$  shielding and initial measurements of the instrument background indicated higher rates than predicted from ground-based testing and simulations.<sup>11</sup> Fluorescence lines from the shielding materials and their respective intensities in the instrument background have been observed to be higher than expected. The cause has been speculated to be impurities in the graded- $Z$  materials, specifically beryllium.<sup>11</sup> This result means that impurities in graded- $Z$  shielding materials for future instruments, such as the Wide Field Imager (WFI) on the Advanced Telescope for High Energy Astrophysics (Athena) mission, should be investigated in simulations before the final selection from suppliers. Reducing the instrument background level for the WFI is currently an active ongoing task within the background working group of the Athena WFI, to meet science operation goals. Therefore, understanding the relationship of impurities in bulk materials with the instrument background is vital.

This paper investigates impurity levels in bulk materials used in graded- $Z$  materials considered for use in future space missions. The impact on the instrument background from the impurities is evaluated through simulations. Where typically the bulk materials use the default materials in the simulation toolkits that are considered “pure,” pure materials offer much faster computational times than those with impurities. Simulations may take a day with a pure material in comparison to days to weeks with impurities depending on the number of impurities. The impurities’ fluorescence line intensities are assessed with their percentage weighting inside the bulk materials. The deposit location of the impurities in the bulk materials is also explored.

## 2 Space Radiation Environment

The space radiation environment varies with location and time. The interactions of a spacecraft with this environment are the main contributor to the instrument background observed. This paper considers a mission based at the Earth–Sun Lagrangian point (L2), which is the orbital location of the eROSITA mission and the candidate orbit for the Athena mission. A representative selection of the radiation environment sources is required for simulations. Including a large number of sources can increase simulation time without adding much value to the end results, due to having only small contributions to the total instrument background.

L2 is 1.5 million kilometers from Earth and is thus outside the local Earth radiation environment clear of the Van Allen trapped particle environment. A mission at L2 or L1 can be considered similar to interplanetary space. This is because the main radiation sources, which contribute to the majority of the instrument background are from solar and cosmic origins. The solar protons from the Sun are quiescent and their intensity increases with solar activity. When solar activity is high, flaring events can occur and the flux intensity of solar protons increases. The high fluxes can make observations difficult, and missions, such as SMILE, have

planned operational safe modes for such events.<sup>12</sup> Due to observation difficulties and the stochastic nature of the solar proton source, the component is not considered when modeling the instrument background.

The two cosmic radiation environment sources are galactic cosmic rays (GCRs) and the cosmic x-ray background (CXB). GCRs include a wide range of particle types. However, the majority are hadrons (~98%). The bulk of the hadronic component is formed of bare hydrogen nuclei (89%), and the other main component is formed of alpha particles (~10%). The heavier hadronic ionic nuclei only account for 1% of the GCR spectrum.<sup>13</sup> The bare hydrogen nuclei, often referred to as GCR protons, are predicted to cause more than half on the instrument background due to their high energies. The instrument background from the alpha component of GCRs is an order of magnitude less than that of the protons. A very small contribution of the instrument background is from the heavier ions, which is attributed to their relatively low flux. Due to this, they are often not modeled. However, their importance remains an open and ongoing topic of research. The largest non-hadronic component of GCR spectra is electrons. Their contribution to the instrument background is similar to that of the GCR alpha particles.

The CXB is a diffuse photon source and spans over a large energy range, from eV to over 100 GeV, and the flux decreases with increasing energy. High-energy photons above 30 keV can fully penetrate the spacecraft shielding and directly interact with the detectors onboard a spacecraft. However, its contribution is much smaller than that of GCR ions.

The L2 environment also includes a small flux of trapped electrons due to the reach of the Earth's magnetic field. However, this source is considered minimal and is often not included when simulating an L2 orbit.

The spectra used in the simulations presented in this document represent the L2 orbit during solar minima over a 5-year period starting in 2030. This is where the GCR sources will be at their strongest due to their link with the solar cycle.

### 3 Passive Shielding Solutions

Passive radiation shielding involves positioning a material or materials in between a radiation source and a radiation-sensitive component. The materials are designed to scatter and absorb the radiation, reducing the probability of reaching the component. This is a common technique used on Earth to shield against radiation sources, with rooms lined with lead in hospitals for radiation-based diagnostics to water used to shield neutrons from nuclear reactors.

These passive bulk shielding solutions have inherent mass problems for use in spacecraft design where the cost for mass to orbit is high, although the new space sector is bringing down the cost to orbit with partially and fully reusable spacecraft, such as Rocket Lab's Electron and SpaceX's Falcon 9 and Starship rockets.<sup>14</sup> This does not solve the passive shielding problem due to the nature of space radiation. The radiation sources are omnidirectional and vary in particle composition and energy. Therefore, a multipurpose solution that mitigates against all sources is difficult to develop.

Aluminum is a common spacecraft structural material that also acts as passive shielding. This is often used as a primary proton shield where the majority of the instrument background arises. However, the protons that interact with the shield produce many secondary particles that also contribute to the instrument background. Therefore, the aluminum proton shield is coupled with other shielding solutions to mitigate against these additional particles.

#### 3.1 Graded-Z Shielding

A graded-Z shielding solution involves selecting a range of materials with varying effective atomic numbers  $Z$  and layering them around radiation-sensitive regions. Often, the shielding is placed in a gradient configuration with the highest- $Z$  material closest to the radiation source and the lowest- $Z$  material near the radiation-sensitive components. Each successive lower- $Z$  layer absorbs the fluorescence from the previous layer reducing the number of particles at each layer. For an x-ray detector, such as a CCD, this configuration can either reduce the x-ray fluorescence, move the fluorescence peak energies outside of the ROI energy window, or both.

### 3.2 Composite Materials

Composite materials are currently being explored as a radiation shielding solution.<sup>15</sup> These often involve producing layers of plastics with additives of high-Z different materials.<sup>16</sup> This can create a more efficient shielding layer while having the mass of a lower-Z material. The layering of these composites has also been explored and combined with the graded-Z approach.<sup>17</sup>

## 4 Simulation Environment

The Geant4 toolkit has been used to simulate the radiation-induced background for the graded-Z shielding investigations. The toolkit was originally designed for high-energy particle physics and has since been expanded and utilized in a variety of applications due to its versatility in simulating the transport of particles as they pass through and interact with matter via Monte Carlo methods.<sup>9</sup> Geant4 is written in C++ and is released under an open-source license.

The simulations presented in this document are produced from an internal tool called the background simulator v1.1, which was developed at The Open University to simulate the radiation instrument background for various missions, such as Athena, SMILE, and THESEUS. The simulation propagates input particle source fluxes through a mass model placed in the center of the environment. Detectors are defined within the mass model. An image preprocessor class providing pixelization operations at simulation run time. The resultant data output includes primary particle information, interaction data, and energy deposited per pixel.

In Geant4, the QBBC physics list was selected as a base for particle and process definitions. The EM physics in the QBBC list was replaced with a modified version of EmStandardPhysics\_SpacePhysics known as the Space Physics User List (SUPL).<sup>18</sup> SUPL includes high-precision EM processes in comparison to the stock EM processes. The modifications applied to SUPL extend the atomic de-excitation processes to include Auger and PIXE in the physics list. Geant4 v10.3.3 has been used in the simulation as the SUPL developed as part of the AREMBES study has been developed against this version.<sup>19</sup> A default cut length of 1  $\mu\text{m}$  is set throughout the simulation with production cuts set from 250 eV to 100 TeV.

The spherical world volume encloses a mass model that describes the geometry. Particles are generated on the surface of the world volume and directed inward. To achieve an isotropic particle flux, that is representative of space radiation environments, particle directions are sampled from a Lambertian distribution. The total number of particles simulated for a mass model is listed in Table 1 unless otherwise stated.

### 4.1 Normalization Procedure

Multiple independent simulations are combined to create a dataset, increasing the statistics improves the error and simulated exposure time. The simulated exposure time is used for normalization and given by

$$t = \frac{N_p}{\Phi \times S_{\text{Enc}} \times \Omega} \text{ s}, \quad (1)$$

where  $N_p$  is the number of simulated particles,  $\Phi$  is the input particle flux, in units of particles/cm<sup>2</sup>/s/sr, and the particle generation region parameters are enclosed surface area  $S_{\text{Enc}}$  and solid angle  $\Omega$ . The input simulation particles are generated on an encompassing sphere where their direction vector is sampled from a Lambertian angular distribution to represent the

**Table 1** Number of simulated particles used in the impurities simulations. These numbers do not reflect the radiation source strengths but rather provide statistical context for the results.

GCR-proton	$5.5 \times 10^6$
GCR-alpha	$3 \times 10^5$
GCR-electron	$1.5 \times 10^8$
CXB	$1.5 \times 10^8$

**Table 2** Thickness of the detector module materials.

Layer	Material	Thickness
OBF	Aluminum	90 nm
Sensor	Silicon	500 $\mu\text{m}$
BCB	Benzocyclobutene	5 $\mu\text{m}$

isotropic nature of the radiation sources. The normalization factor is used for the analysis of the simulations in various calculations, such as the particle rate  $R$ , which is evaluated as  $R = C/t$ , where  $C$  is the number of detected counts.<sup>20</sup> This is used in the background rate predictions. For a flat panel detector with effective front-facing cross-sectional area  $S_{\text{Det}}$ , the background rate is defined as<sup>21</sup>

$$B = R/S_{\text{Det}}. \quad (2)$$

The flat panel detector is sensitive to omnidirectional particles but the results are read out as a pixelated 2D panel analogous to a physical device.

#### 4.2 Mass Models

Mass models describe the simulation geometry, such as material, location, and size of mass objects inside a simulated world volume. The mass models have been designed using FASTRAD<sup>®22</sup> and are exported to a Geometry Description Markup Language file format for use with Geant4.<sup>23</sup> The impact of impurities in the material selection is the focus of the investigation and the mass models have been constructed to simulate a graded-Z shielding application. To remove any geometric artifacts in the simulation output, a spherical shell design was selected. The mass model consists of concentric graded-Z material shells inside a spherical vacuum world volume with an outer diameter of 310 mm. At the center of the mass model, it is a typical detector module containing three material layers. The middle layer is the sensitive silicon layer where readout is performed. The top layer is an aluminum optical blocking filter (OBF), and the bottom layer is a benzocyclobutene (BCB) backing layer. Both the OBF and BCB are common layers used for in-flight detector devices. Table 2 lists the material thickness included in the detector

**Table 3** Spherical mass models reference names and graded-Z configurations.

Model ID	Description
NoImp	Three layers: Al, Mo, and Be. No impurities
ImpBe	Three layers: Al, Mo, and Be. Be material has three impurities
ImpBeFull	Three layers: Al, Mo, and Be. Be material has 10 impurities
BeLow	Three layers; Al, Mo, and Be. Be material has three impurities at low concentrations
ImpMoK	Three layers: Al, Mo, and Be. Mo has three impurities
ImpMoFe	Three layers; Al, Mo, and Be. Mo has three impurities
noBe	Two layers: Al and Mo. No impurities
SandwichBeFe	Three: layers: Al, Mo, and Be. Three impurities concentrated at the surface in Be
SandwichBeLow	Three layers: Al, Mo, and Be. Three impurities with low concentrations in Be. Impurities are concentrated at the surface
SandwichBeMoK	Three layers: Al, Mo, and Be. Three impurities concentrated at the surface in Mo
SandwichnoBe-impMoK	Two layers: Al and Mo. Three impurities concentrated at the surface in Mo
SandwichnoBe-impMoFe	Two layers: Al and Mo. Three impurities concentrated at the surface in Mo

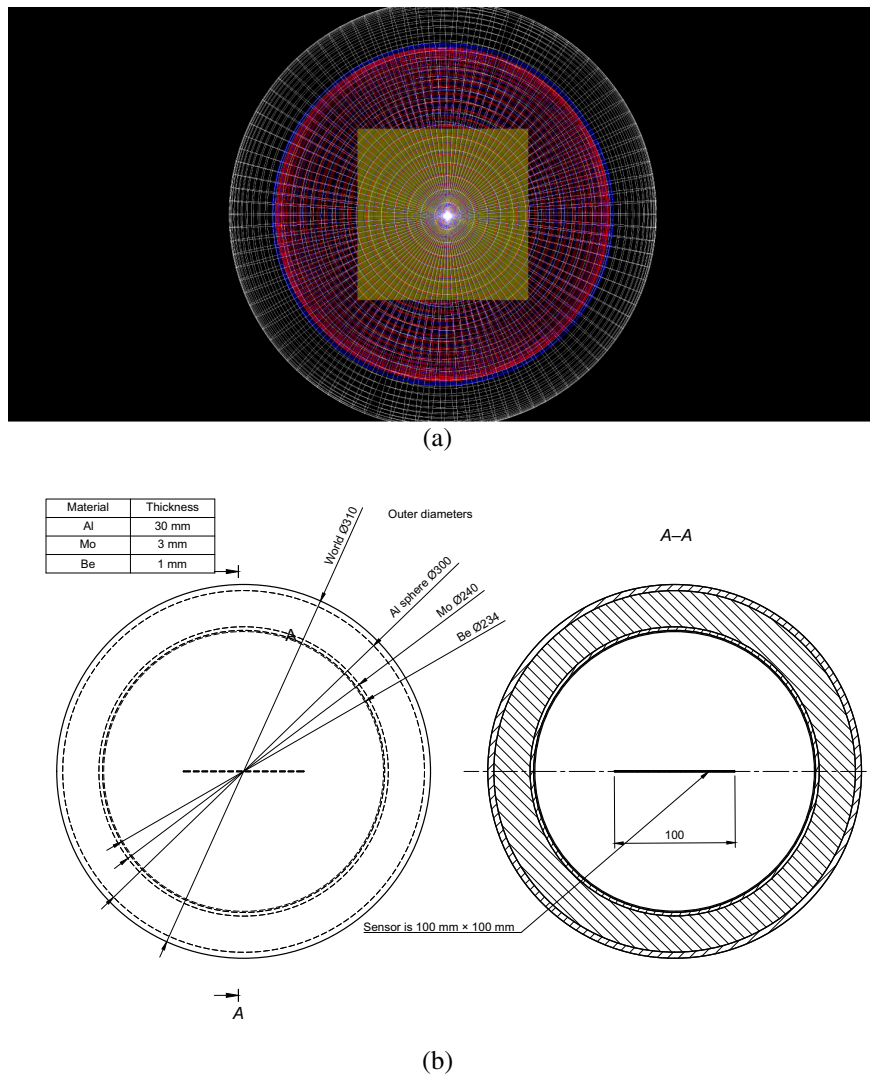


**Fig. 1** Images of mass model definitions and set-up in Geant4. (a) View of set-up in Geant4 simulation. (b) Diagram of the spherical shells in the simulation mass model. Unlabeled regions between volumes are modeled as a vacuum.

module. Each layer in the module measures 100 mm × 100 mm in the plane. Figure 1 depicts the mass model construction used for the simulations. The regions between the labeled investigated shielding material regions are set to vacuum within the simulations. Mass model identifiers and descriptions are provided in Table 3.

### 4.3 Impurity Configurations

A review of manufacturers' data sheets and published literature for common graded-Z materials revealed common impurities, which have fluorescence lines below 10 keV. These could potentially cause problems within missions that have a science ROI, in this energy band, e.g., Athena WFI.

Geant4 has a library of default material definitions, these are used as a baseline for comparison in the mass models. The detector assembly contains both aluminum and silicon, these use the default Geant4 definitions and are not altered to include any impurities. As the focus of this work is on the instrument background from the shielding, impurities, and dopants inside the representative silicon detector were not included in the study. The three graded-Z shielding material definitions (Al, Mo, and Be), by default, contain no impurities and are 100% pure. Impurities in the low-Z molybdenum and beryllium layers are altered for different simulations.

**Table 4** Impurities for the beryllium materials.

Element	Percentage loading
(a) Impurities loading for ImpBeFull	
Cu	0.02
Cr	0.02
Ca	0.02
Ni	0.04
Al	0.06
Si	0.06
Zn	0.08
Mg	0.10
C	0.16
Fe	0.16
Be	99.28
(b) Impurities loading for ImpBe	
Ca	0.02
Ni	0.04
Fe	0.16
Be	99.78
(c) Impurities loading for BeLow	
Ca	0.01
Ni	0.02
Fe	0.08
Be	99.89

The Geant4 physics processes calculate the interaction cross sections based on the percentage loadings of each material. Therefore, as a result, the impurities are homogeneously distributed throughout the bulk material.

A selection of models with varied impurity concentrations for the two low- $Z$  materials was created. Impurity levels for three different beryllium material definitions are summarized in Table 4.

The beryllium impurities are based on those listed in the manufacturer's data sheet of the Be used for the eROSITA mission. Some trace impurities with low levels have been removed  $\lesssim 0.01\%$ . The loading of the remaining impurities percentage loadings was doubled. This increases the probability of detection and thus gives an indication that impurities make a difference. The model including all these modified impurities is known as ImpBeFull. Two additional Be impurity models were created with a limited number of impurities. Impurities with fluorescence energies not in or close to the Athena scientific ROI were removed.

The ImpBe model keeps the percentage loading of the impurities while increasing the base bulk material weighting. Another model referred to as the BeLow model includes the impurities without the double weighting. Therefore, this material description is more representative of that flown with eROSITA. The beryllium weighting has been scaled to remove the other impurities.

A list of 14 impurities was created from a review of the literature on molybdenum. From this list, impurities were identified, which would potentially impact the WFI science ROI.

**Table 5** Impurities for the molybdenum materials.

Element	Percentage loading
(a) Impurities loading for ImpMoK	
Ni	0.0326
Fe	0.0240
K	0.1225
Mo	99.8209
(b) Impurities loading for ImpMoFe	
Ni	0.0326
K	0.0240
Fe	0.1225
Mo	99.8209

Consequently, two material models were created containing only a select few impurities. These are referred to as ImpMoK and ImpMoFe models. The difference between the models is the percentage loadings between the materials, a comparison between these two models is shown in Table 5.

#### 4.4 Impurity Sandwiches

The distribution of impurities is often not listed in manufacturers' data sheets, and it is assumed that they are uniformly distributed throughout the bulk. There is a possibility that some impurities are caused by manufacturing techniques, for example, from tooling of the material to achieve desired thickness or from the molds used for casting the materials. Therefore, the outer surfaces of the materials used may have increased or different impurity levels. The thicknesses of the impurity layers do not represent physical phenomena, such as diffusion, machining, or casting. The models are designed to investigate if impurities concentrated near the surface can alter the instrument background. Several models were developed to test if impurities being part of the outer surface only would have any subsequent impact on the radiation background spectra observed. These models are referred to as "Sandwich" models because the material is split into three layers labeled: bottom, middle, and top. The bottom layer is closest to the sensor in the mass model. The bottom and top layers are the outer layers and contain the same percentage impurities. To investigate the scenario where the impurities only arise from tooling, the middle layer is set to be 100% pure with the impurities only in the outer layer.

The outer surface layers are defined as 20% of the material thickness with 10% assigned to the top and bottom layers, respectively. Therefore, as the beryllium material is 1 mm thick, the outer layers are 0.1 mm each with the middle layer as 0.8 mm. The molybdenum layer is thicker at 3 mm, thus its middle layer is 2.4 mm thick, and its outer layers are 0.3 mm. The impurities are then concentrated into the outer layers at 5 times the homogeneous distribution level such that the same overall mass of impurities remains comparable to the homogeneous materials. The breakdown of impurities is listed in Tables 6 and 7.

## 5 Background Analysis

Two key parameters are calculated from the simulations to determine the impacts of the impurities in the base shielding material layers. The background rate for a particle source over an energy window  $E_{\text{window}}$  is calculated using

$$B_P = \frac{1}{tA_{\text{sensor}}E_{\text{window}}} \left( C_{P,\text{En}} \pm \sqrt{C_{P,\text{En}}} \right), \quad (3)$$

**Table 6** Impurities for the beryllium sandwich models.

Element	Percentage loading	
	Middle layer	Outer layer
(a) Impurities loading for the different layers of the SandwichBeFe model		
Ca	0	0.1
Ni	0	0.2
Fe	0	0.8
Be	100	98.9
(b) Impurities loading for the different layers of the SandwichBeLow model		
Ca	0	0.05
Ni	0	0.10
Fe	0	0.40
Be	100	99.45

**Table 7** Impurities for the molybdenum sandwich models.

Element	Percentage loading	
	Middle layer	Outer layer
(a) Impurities loading for the different layers of the SandwichMoK model		
Ni	0	0.6125
Fe	0	0.1200
K	0	0.1630
Mo	100	98.1054
(b) Impurities loading for the different layers of the SandwichMoFe model		
Ni	0	0.6125
Fe	0	0.1630
K	0	0.1200
Mo	100	98.1054

where  $t$  is the time normalization defined in Eq. (1),  $A_{\text{sensor}}$  is the surface area of the sensor, and  $C_{P,\text{En}}$  is the number of counts from a particle source within the energy window. The individual particle source background rates are combined for a total background rate value. For the studies presented in this paper,  $A_{\text{sensor}}$  is equivalent to  $S_{\text{det}}$  in Eq. (2) but can be altered to different areas when regions of detectors are explored, such as readout nodes, during post-processing.

Fluorescence lines can partially inflate the calculated background rates if they are contained within the energy window. Individual analysis of the lines is utilized to determine their associated impact. The fluorescence line height is calculated using

$$H = E_{LW}[(F_L - B_A) \pm \sqrt{F_L + \sigma_B^2}], \quad (4)$$

where  $E_{LW}$  is the energy window of the  $F_L$  bins, in units of counts  $\text{cm}^{-2} \text{s}^{-1}$ . The background around the fluorescence is used as a baseline for the line intensity calculation. In the equation,  $B_A$

is the arithmetic mean of adjacent bins to the line energy, and  $\sigma_B$  is the standard deviation of the selected background bin and is used as the error. Line height parameters are calculated for base material fluorescence lines and impurity fluorescence lines in and close to the region of impact to assess the impurities' impact on the instrument background.

## 6 Results and Discussion

Here, the results from the different material impurity configurations for beryllium and molybdenum are reported. The impurities are assumed to be distributed homogeneously throughout the bulk material. The background spectral results are those that could occur if the spherical model were placed in an L2 orbit, where the environment is described in Sec. 2.

### 6.1 Beryllium

The three beryllium configuration models are compared in Fig. 2 alongside the “no impurities” model. The no impurities model provides a baseline for all the simulations, as there are no additional impurities added. Therefore, these materials can be considered “pure” as they use default Geant4 material presets of their elemental namesake, i.e., they appear in standard simulation practice form. The iron  $K\alpha$  6.4 keV fluorescence line is not present in the baseline no impurities model. However, it is present in all of the beryllium impurities configuration models where the percentage loading ranges from 0.08% to 0.16%. These simulation results demonstrate that even a small percentage loading of the bulk material with impurities will have a significant impact on the observed spectrum.

The Fe  $K\alpha$  line heights are listed in Table 8. The baseline no impurities model has a line height of  $(-8 \pm 33) \times 10^5 \text{ cm}^{-2} \text{ s}^{-1}$ . This result indicates that there is effectively no fluorescence

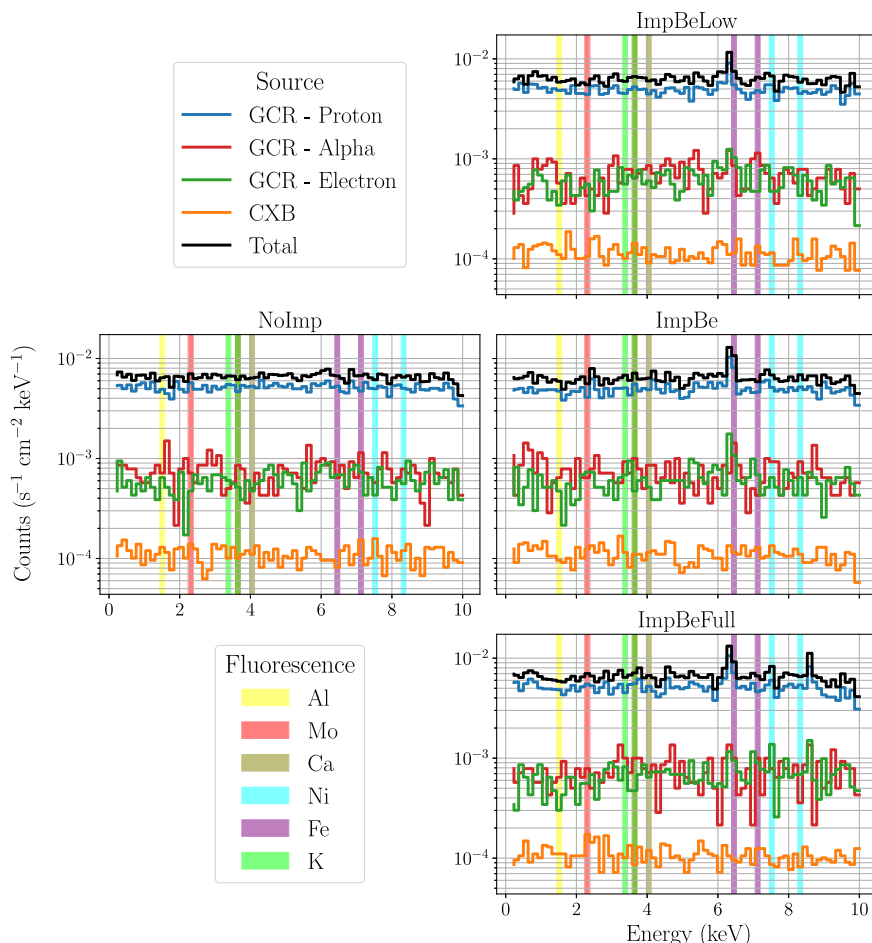


**Fig. 2** Comparison of the molybdenum low-impurity runs.

**Table 8** Background spectra metrics for the different beryllium materials.

	NoImp	ImpBeFull	ImpBe	BeLow
Fe $K\alpha$ line height ( $\times 10^{-3} \text{ cm}^{-2} \text{ s}^{-1}$ )	$-0.08 \pm 0.33$	$1.29 \pm 0.40$	$1.44 \pm 0.35$	$0.83 \pm 0.37$
Mean background rate in the 2 to 7 keV region ( $\times 10^{-3} \text{ cm}^{-2} \text{ keV}^{-1} \text{ s}^{-1}$ )	$6.66 \pm 0.09$	$6.88 \pm 0.09$	$6.64 \pm 0.09$	$6.41 \pm 0.09$

line in this region, as the line height is  $<0$  and there is a high error. Analyzing the background spectra in Fig. 2 demonstrates that in the Fe  $K\alpha$  energy region the signal is noisy. This is partially due to simulation statistics but also due to this region being in the background continuum where there is no underlying spectral features present. In contrast, the beryllium models have the fluorescence spectral feature at this point. Therefore, the origin of the 6.4 keV fluorescence line is directly from the impurities added to the simulated material as this is the only difference between the no impurity and other models.

The impBe model is a cut-down model of the impBeFull impurity list. The data presented in Table 8 show that the Fe  $K\alpha$  line height between the two models is within error, whereas the mean background rate for the full impurity model is higher than the reduced model. This is in part expected as some of the higher-Z impurities have been removed. These would increase the production of secondaries from the interactions and populate the background continuum. Therefore, the impBe is a good representation of impBeFull for studies investigating fluorescence line presence and intensity.

As Fig. 2 demonstrates, the background spectra for the full model (ImpBeFull) also includes the Zn 8.64 keV fluorescence line. However, this would be outside the Athena WFI science ROI of 2 to 7 keV. The Ni 7.48 keV fluorescence line is also present in this configuration, although, it is within error of the background continuum.

The BeLow model investigates how reducing the impurity weightings impacts the background spectra. The model contains half the percentage impurities as the impBe mode. The BeLow measured Fe line height is approximately a reduction of a factor of 1.7 in comparison to the impBe model. However, the values are within  $2\sigma$ . Therefore, choosing materials based on their impurity loading could be advisable if the impurities have the potential of fluorescing in the ROI.

Table 8 summarizes two metrics used to evaluate the instrument background: the fluorescence line heights and the background rate. The background rate in the Athena WFI science ROI, across all the models, is within  $3\sigma$ . The beryllium material with full impurities (ImpBeFull) does appear to increase the rate, due to the impurities having a higher-Z causing more scattering events. This in turn increases the number of secondaries produced with lower energies, which have a higher probability of depositing energy in the sensor. Both the smaller impurity models, impBe and BeLow, have a background rate lower than the no impurities (noImp) model. However, the impBe model is within 1 standard error of the noImp data. Conversely, the difference between the BeLow and noImp results is close to  $3\sigma$ . This may suggest that loading the bulk material with small levels of impurities, of higher Z than the bulk, may aid in the overall reduction of the background rate. Higher energy photons, which would normally not be absorbed by the bulk low-Z beryllium, are instead absorbed by the higher-Z impurities leading to a decrease in instrument background. However, the impurities act as scattering centers for other higher energy particles potentially increasing the number of lower energy secondary radiations and thus increasing the background rate. Therefore, this suggests that there is a point where the percentage loading of impurities may produce too many secondaries leading to an increased background rate. The results also show that the impurity loading is synonymous with the composite material shielding approach, where high-Z materials are suspended in a low-Z structural material.

## 6.2 Molybdenum

The molybdenum layer sits between the aluminum and the low-Z beryllium layer. Any secondaries produced from interactions with the molybdenum layer have the potential to be absorbed in the low-Z layer of this graded-Z shielding configuration. The observed background spectra for

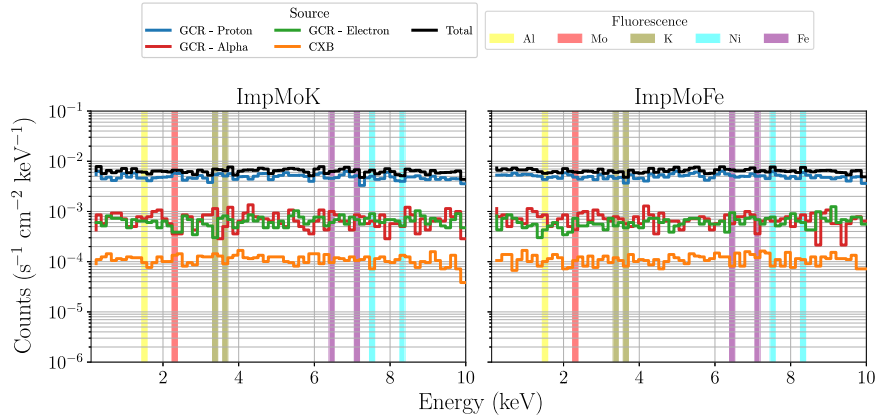


**Fig. 3** Comparison of the molybdenum low-impurity model runs.

**Table 9** Background spectra metrics comparison among nolmp, impMoK, and impMoFe.

	Nolmp	ImpMoK	ImpMoFe
Fluorescence line height ( $\times 10^{-3} \text{ cm}^{-2} \text{ s}^{-1}$ )			
K 3.314 keV	$-0.02 \pm 0.15$	$-0.11 \pm 0.30$	$0.05 \pm 0.31$
K 3.59 keV	$0.04 \pm 0.25$	$0.10 \pm 0.33$	$-0.16 \pm 0.25$
Fe 6.40 keV	$-0.08 \pm 0.33$	$-0.22 \pm 0.34$	$0.04 \pm 0.30$
Fe 7.06 keV	$0.05 \pm 0.31$	$0.02 \pm 0.34$	$0.03 \pm 0.28$
Ni 7.48 keV	$-0.10 \pm 0.27$	$0.07 \pm 0.32$	$0.09 \pm 0.28$
Ni 8.27 keV	$0.06 \pm 0.28$	$-0.35 \pm 0.24$	$0.11 \pm 0.26$
Mean background rate in the 2 to 7 keV region ( $\times 10^{-3} \text{ cm}^{-2} \text{ keV}^{-1} \text{ s}^{-1}$ )	$6.66 \pm 0.09$	$6.51 \pm 0.08$	$6.47 \pm 0.08$

the ImpMoK and ImpMoFe models are compared in Fig. 3. The spectra between the two are very similar and both lack strong fluorescence lines. This is reflected in the data shown in Table 9, which summarizes the background rate and fluorescence line heights. The metrics demonstrate that both the ImpMoK and ImpMoFe data are within the error of the control model without impurities.

The impurities in the molybdenum do not appear to impact the spectral results. This is partly due to the low  $Z$ , beryllium layer absorbing the particles associated with the fluorescence mechanism.

The tabulated data also show that having a small percentage of impurities decreases the background rate, this is similar to the results shown in the beryllium impurity simulations. The cause of this might be the higher- $Z$  impurities cause more scattering and the subsequent secondary particles produced are absorbed into the surrounding lower- $Z$  layer.

To directly investigate the molybdenum layer, the low- $Z$  beryllium layer was removed in a series of simulations. Due to no longer being in a graded- $Z$  configuration, the background rate increased as expected. However, the impurity fluorescence lines were not observable in the spectra due to self-absorption in the molybdenum, as Fig. 4 demonstrates. Figure 4 compares the transmission probability for 1 mm of the two graded- $Z$  materials. The sharp drop in transmission probability at 20 keV for the molybdenum is due to the proximity of the K-edge. The transmission of particles below 15 keV is essentially 0 through 1 mm of molybdenum. Therefore, the Fe  $K\alpha$  line at 6.4 keV would partially transmit in the beryllium and be self-absorbed in the molybdenum. Thus the location of the impurities dispersed within the bulk material will also impact the strength of the impurity lines. Impurities deposited near the surface facing toward the detector are more likely to impact the instrument background.

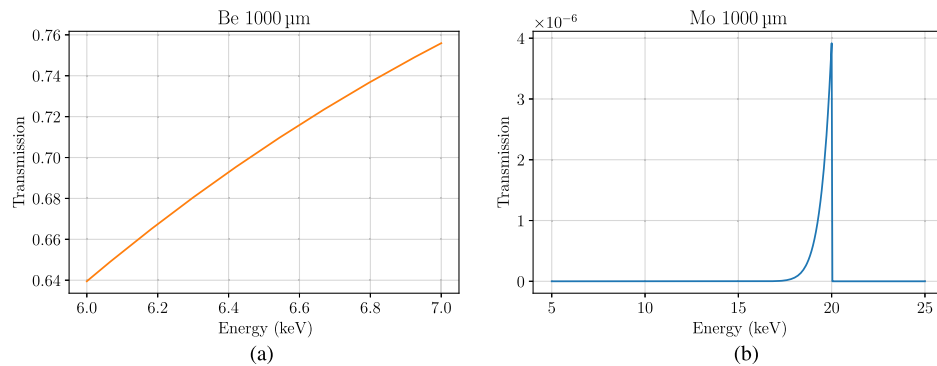


**Fig. 4** Self-absorption of x-rays within beryllium and molybdenum. Plots generated using data from the center for x-ray optics.<sup>24</sup> (a) Beryllium x-ray transmission probability. (b) Molybdenum x-ray transmission probability.

### 6.3 Distribution of Impurities

The materials defined using Geant4 assume that each compositional element or compound is homogeneously distributed throughout the geometry of the volume the material is assigned to. Due to manufacturing techniques, there is a possibility that the impurities in the materials could be distributed in different regions of the material, for example, impurities may be concentrated in the outer surfaces due to machining. Figure 4 shows that lowering the material thickness can increase the transmission probability of fluorescence lines.

The beryllium models were simulated in a sandwich configuration where the net percentage loading was kept the same, but the impurities have been concentrated to the outer surfaces. The background rate and fluorescence line heights for the impurities are listed in Table 10. The results for the iron fluorescence lines are within error of each other. This is because the majority of the observed fluorescence lines originate from the concentrated region close to the detector, with the impurities concentrated on the far side having a reduced transmission probability.

Comparing the sandwich and homogeneous layouts shows that the background rate is higher for the sandwich configuration, although the differences are within  $2\sigma$ . As the impurities are concentrated on the outer surfaces, the probability of absorption of the secondaries produced from interactions with the impurities is reduced. Therefore, these are more likely to be detected by increasing the overall background rate. The Sandwich BeFe model had a higher background rate than the no impurities model. Therefore, the location of the percentage loading does alter the background rate. This suggests that the bulk material is reabsorbing secondaries produced. When the impurities are concentrated on the outer surfaces, there is less bulk to reabsorb the secondaries on the near outer surface.

Similar to the homogeneous distribution model, there is not much difference between the molybdenum sandwich and the no impurities model due to the low- $Z$  layer included in the simulation. The background rate for the sandwich impMoK is  $(6.57 \pm 0.09) \times 10^{-3} \text{ cm}^{-2} \text{ keV}^{-1} \text{ s}^{-1}$ , which is within error of both the noImp and ImpMoK results listed in Table 9. Removing the low- $Z$  beryllium layer also showed similar results for the sandwich and

**Table 10** Comparison of the background spectra metrics for the different beryllium material models.

	ImpBe	Sandwich BeFe	BeLow	Sandwich BeLow
Fe 6.4 keV line height ( $\times 10^{-3} \text{ cm}^{-2} \text{ s}^{-1}$ )	$1.44 \pm 0.35$	$1.42 \pm 0.35$	$0.83 \pm 0.37$	$0.91 \pm 0.35$
Fe 7.06 keV line height ( $\times 10^{-3} \text{ cm}^{-2} \text{ s}^{-1}$ )	$-0.16 \pm 0.29$	$0.28 \pm 0.31$	$0.02 \pm 0.30$	$0.12 \pm 0.30$
Mean background rate in the 2 to 7 keV region ( $\times 10^{-3} \text{ cm}^{-2} \text{ keV}^{-1} \text{ s}^{-1}$ )	$6.64 \pm 0.09$	$6.80 \pm 0.09$	$6.41 \pm 0.09$	$6.57 \pm 0.09$

**Table 11** GCR: proton background spectra metrics for the sandwich models with the low-Z beryllium layer removed.

	Sandwich		
	noBe	noBe-impMoK	noBe-impMoFe
Mo 2.29 keV $L\alpha$ line height ( $\times 10^{-3} \text{ cm}^{-2} \text{ s}^{-1}$ )	$3.38 \pm 0.68$	$3.52 \pm 0.88$	$2.88 \pm 0.73$
K 3.314 keV line height ( $\times 10^{-3} \text{ cm}^{-2} \text{ s}^{-1}$ )	$0.21 \pm 0.18$	$-0.04 \pm 0.21$	$-0.07 \pm 0.15$
Fe $K\alpha$ line height ( $\times 10^{-3} \text{ cm}^{-2} \text{ s}^{-1}$ )	$-0.03 \pm 0.17$	$0.10 \pm 0.14$	$-0.03 \pm 0.13$
Mean background rate in the 2 to 7 keV region ( $\times 10^{-3} \text{ cm}^{-2} \text{ keV}^{-1} \text{ s}^{-1}$ )	$6.73 \pm 0.10$	$6.63 \pm 0.10$	$6.57 \pm 0.10$

homogeneous impurity layouts, this is shown in Table 11. There is no difference within error for the fluorescence line heights. The background rate is lower for the impurity models than the no impurity baseline model, although these are also within error.

In summary, the distribution of low percentage loading of impurities ( $\approx 0.1\%$ ) with the material thicknesses simulated does not have a large impact on the background rate of fluorescence line intensity. The background rate for the sandwich beryllium models did increase compared to the homogeneous models, but the opposite was observed for the molybdenum simulations. Therefore, different outcomes can arise depending on the bulk material. Future work is planned to investigate the distribution of surface impurities in materials and compare simulations with experimental data.

## 7 Conclusions

Impurities in graded-Z shielding materials have been simulated and their impact on the radiation-induced background within the example of a science 2 to 7 keV ROI, similar to that of the Athena WFI instrument, have been analyzed. Simulations were conducted on a model that had three concentric spherical shell layers with a square planar silicon sensor placed in the center. The shells represented a graded-Z shield consisting of aluminum, molybdenum, and beryllium. The beryllium layer was closest to the sensor. The radiation background was simulated using four different sources; protons, electrons, helium nuclei, and photons. The first three correspond to the components from the GCR and the photons are drawn from a distribution that represents the CXB.

A model using the default Geant4 simple pure materials, G4\_Be and G4\_Mo, was used as a baseline for comparison. Common impurities were identified for molybdenum and beryllium. Common impurities for the graded-Z materials were collated from data sheets and literature. Impurities with high percentage loadings and fluorescence lines in the science ROI were selected for study. Multiple impurity models were investigated while varying the number of impurities, percentage loading of the impurities in the materials, and impurity location in the bulk material. All percentage loadings were of the order 0.1% or lower.

Primary simulations focused on impurities distributed homogeneously through the base material. Simulations of the beryllium impurities revealed that models containing a few key impurities were representative with regards to the fluorescence lines of a model including a large selection of impurities. Two reduced impurity models containing a factor of 2 difference in percentage loading were tested and compared. The results revealed that the fluorescence line scales approximately with percentage loading, with a factor of 1.7 difference observed. The background rate was compared across all the impurity models to the baseline. This revealed a 3% higher background rate for the full impurity model when compared to the baseline, although, this was within a  $2.5\sigma$  error. Conversely, the reduced impurity models had lower background rates, one was within  $1\sigma$  error and the other within  $3\sigma$  error. This is caused by the high-Z impurities acting as scattering centers for higher energy particles that traverse through the bulk beryllium to interact. These interactions cause the production of more low-energy secondary particles that are reabsorbed back into the surrounding bulk material. In the model where many impurities exist,

the bulk material does not reabsorb all of the secondaries produced and thus they pass through and are detected; whereas for the reduced impurity models, there is still enough bulk material to reabsorb the secondaries produced. Therefore, there may be an optimal impurity concentration that aids in the reduction of detectable particle background in the science ROI. Simulations of impurities in the molybdenum did not reveal the presence of fluorescence lines. This was determined to be due to the low transmission of the fluorescence photons within the bulk molybdenum material from self-absorption. Analysis of the background rates for molybdenum did show differences with the impurities present. Similar to the beryllium results, impurities in molybdenum lowered the background rate within  $2\sigma$  of the baseline models without impurities. This was observed in simulations both with and without a low-Z beryllium layer.

As the transmission probability of secondaries produced from fluorescence is dependent on the material thickness, additional simulations investigating the impurity location were performed. During the manufacture of the materials, the impurities may be concentrated on the outer layers from casting or tooling for example. Therefore, sandwich model simulations were performed where the overall percentage loading was kept the same, but the impurities were concentrated to the outer 10% of the surfaces and with a middle layer that had no impurities. Simulations were performed on a selection of beryllium and molybdenum impurity configuration models. All the results showed no difference in fluorescence line intensity when compared with their homogeneous impurity distribution counterpart. However, the reason for this may be that half the percentage impurities that are closest to the sensor cause this. The fluorescence from the far impurity region is absorbed by the bulk of the material reducing their contribution. Further investigations would need to be performed to validate this theory.

The background rates, compared to the baseline no impurity model, were all lower as previously seen with one exception. One of the sandwich impurity models had a higher background than the baseline model. This indicates that the location of the impurity alters the background rate, due to secondaries produced from the impurities near the surfaces having less bulk material to reabsorb. Future investigations are planned using surface thickness impurities representative of machining, casting, and diffusion to further study this outcome.

In summary, even a small percentage loading of impurities  $\lesssim 0.15\%$  in the bulk low-Z material can lead to fluorescence lines being observed in the materials simulated, whether it is beryllium, Kapton, or another material. Although, this will be dependent on material choice as some materials will increase background depending on the materials. The addition of impurities also impacts the background rate. The simulations have revealed that a small loading can offer improvements to the background rate as the impurities can scatter higher energy particles allowing the bulk material to absorb the lower energy secondaries produce during the interactions. However, if there are too many impurities the bulk material cannot sustain the absorption, and the rate increases. Simulations have shown evidence supporting this, where concentrating the impurities in a region of the material close to the sensor can increase the background rate. The distribution of impurities in the material is related to manufacturing processes, such as machining. Therefore, at material selection for shielding that is near photosensitive detectors, the impurities in the material should be considered, to prevent increases in instrument background and reduce fluorescence spectral features in observations. Therefore, it is recommended for completeness that impurities are included in low Z level materials and those with a direct line of sight to the focal planes of detectors, such as CCDs and DEPFETs. This will improve instrument background estimates for missions utilizing these detectors.

---

### Code, Data, and Materials Availability

All data in support of the findings of this paper are available within the article. Supporting files that can be used to reproduce the data presented in this article are publicly available in Ref. 25.

### Acknowledgments

The authors would like to thank Emanuele Perinati, (University of Tübingen), for the eROSITA information and discussions. The authors would also like to thank Neil Hollyhoke, (The Open

University), for help with identifying molybdenum impurities. Some of the simulation inputs, codes, and results were undertaken through work funded by UKSA for Athena (Grant No. ST/S006451/1).

## References

1. N. Riva et al., “Study of a superconducting magnetic diverter for the ATHENA x-ray space telescope,” *IEEE Trans. Appl. Supercond.* **28**(4), 1–4 (2018).
2. L. W. Townsend, “Critical analysis of active shielding methods for space radiation protection,” in *IEEE Aerosp. Conf.*, IEEE, pp. 724–730 (2005).
3. G. Malaguti et al., “Active and passive shielding design optimization and technical solutions for deep sensitivity hard x-ray focusing telescopes,” *Proc. SPIE* **5900**, 59000M (2005).
4. W. C. Fan et al., “Shielding considerations for satellite microelectronics,” *IEEE Trans. Nucl. Sci.* **43**(6), 2790–2796 (1996).
5. W. Atwell et al., “Mitigating the effects of the space radiation environment: a novel approach of using graded-Z materials,” in *AIAA SPACE 2013 Conf. and Exposition*, p. 5385 (2013).
6. E. Perinati et al., “The radiation environment in L-2 orbit: implications on the non-X-ray background of the eROSITA pn-CCD cameras,” *Exp. Astron.* **33**(1), 39–53 (2012).
7. N. Gehrels et al., “The Swift gamma-ray burst mission,” *Astrophys. J.* **611**(2), 1005 (2004).
8. T. Eraerds et al., “Enhanced simulations on the Athena/Wide Field Imager instrumental background,” *J. Astron. Telesc. Instrum. Syst.* **7**(3), 034001 (2021).
9. J. Allison et al., “Recent developments in Geant4,” *Nucl. Instrum. Methods Phys. Res., Sect. A* **835**, 186–225 (2016).
10. C. Ahdida et al., “New capabilities of the FLUKA multi-purpose code,” *Front. Phys.* **9**, 788253 (2022).
11. P. Predehl et al., “The eROSITA X-ray telescope on SRG,” *Astron. Astrophys.* **647**, A1 (2021).
12. G. Branduardi-Raymont et al., “SMILE definition study report (Red book),” (2018).
13. V. Bothmer and I. Daglis, *Space Weather: Physics and Effects*, Springer Praxis Books, Springer Berlin Heidelberg (2007).
14. H. Jones, “The recent large reduction in space launch cost,” in *48th Int. Conf. Environ. Syst.* (2018).
15. M. Naito et al., “Applicability of composite materials for space radiation shielding of spacecraft,” *Life Sci. Space Res.* **31**, 71–79 (2021).
16. M. Steffens et al., “Characterization of novel lightweight radiation shielding materials for space applications,” *IEEE Trans. Nucl. Sci.* **64**(8), 2325–2332 (2017).
17. J. Wrobel et al., “Versatile structural radiation shielding and thermal insulation through additive manufacturing,” in *27th Annu. AIAA/USU Conf. Small Satellites* (2013).
18. P. Dondero and A. Mantero, “A ‘space dedicated’ GEANT4 physics list from the AREMBES project,” in *12th Geant4 Space Users Workshop* (2017).
19. V. Ivanchenko et al., “Validation of Geant4 10.3 simulation of proton interaction for space radiation effects,” *Exp. Astron.* **44**(3), 437–450 (2017).
20. V. Fioretti, S. Lotti, and G. Santin, “AREMBES WP 7: normalization of an isotropic flux in space in Geant4 simulations,” Tech. Rep., AREMBES\_Geant4, ESA AREMBES (2018).
21. S. Lotti et al., “Estimates for the background of the Athena X-IFU instrument: the cosmic rays contribution,” *Proc. SPIE* **10699**, 106991Q (2018).
22. J.-C. Thomas et al., “FASTRAD: a 3D CAD interface for radiation calculation and shielding,” in *11th Int. Conf. Radiat. Shielding (ICRS-11)* (2008).
23. R. Chytráček et al., “Geometry description markup language for physics simulation and analysis applications,” *IEEE Trans. Nucl. Sci.* **53**(5), 2892–2896 (2006).
24. T. C. for X-Ray Optics, “X-ray interactions with matter-filter transmission,” [https://henke.lbl.gov/optical\\_constants/filter2.html](https://henke.lbl.gov/optical_constants/filter2.html) (accessed 22 February 2021).
25. M. Hubbard, “Impurities\_JATIS\_Paper: initial release (data),” *Zenodo*, 8 June 2023, <https://doi.org/10.5281/zenodo.8018064>.

**Michael W. J. Hubbard** is a space radiation environment scientist at the Centre of Electronic Imaging, The Open University, United Kingdom. He assesses the potential radiation environment for future space missions and models the subsequent impacts, such as dose and instrument background rates. Their expertise revolves around the design of Geant4 simulations and data analysis pipelines for radiation detectors. He has a background in scintillation detector technology utilizing pulse shape discrimination for neutron detection.

**David Hall** is a senior lecturer in physical sciences at The Open University. Over the last 15 years, he has worked on the simulation of instrument background, studying the background on XMM-Newton, Swift, and Suzaku. He is currently involved in the background predictions

for the SMILE and THESEUS SXI instruments alongside the Athena WFI, particularly the study of graded-Z radiation shielding and the validation of Geant4 for instrument background simulations.

**Andrew Holland** is a professor in physical sciences at The Open University. Over the last 30 years, he has worked on development of detectors and instrumentation for space science and has worked on XMM-Newton and Swift, and also studied instrumentation for IXO and Athena. He is currently developing X-ray instrumentation for the SMILE and THESEUS SXI instruments and working on development of new CMOS X-ray image sensors for new space science applications.

Biographies of the other authors are not available.